Optimization of Computational Control-Parameter Values for Dynamic Optical Tomographic Image Reconstruction

Harry L. Graber[1], Stephanie Y. Lum[2], Yong Xu[1], and Randall L. Barbour[1]
[1]*SUNY Downstate Medical Center*, [2]*Carnegie-Mellon University*

BACKGROUND and INTRODUCTION

When processing optical tomographic measurement data, the issue of data integrity is particularly important owing to the sensitivity of reconstructed image accuracy to various types of data errors. Specific examples of some of the measurement-related issues that arise when data are collected using our group's previously described dynamic imager[1], for the case of a measurement on the forearm of a volunteer (Figure 1), are shown in Figure 2. Selected raw-data time series are plotted in each panel. The reduction in signal-to-noise ratio (SNR) of the data with increasing distance between source and detector, that is illustrated in Fig. 2(a) points to the practical necessity for developing criteria for deciding which channels are excessively noisy and accordingly should be deleted from a data set. A second potential problem is the appearance of an appreciable difference between signals that are recorded by "conjugate" S-D channels (i.e., source *a*, detector *b* vs. source *b*, detector *a*), which ought to be equal according to the principle of reciprocity[2] (Fig. 2(b)). A third is the appearance of differences in scale between the data recorded in conjugate channels (Fig. 2(c)). Some of the observed differences can simply be attributed to the channels having different gain settings or DC offset levels, while in other cases they persist even after these instrumentational factors are taken into account. These latter phenomena (among others not explicitly illustrated here) point to a necessity for developing criteria for deciding whether the data time-series for each conjugate pair are sufficiently similar that the measurement can be regarded as "trustworthy."

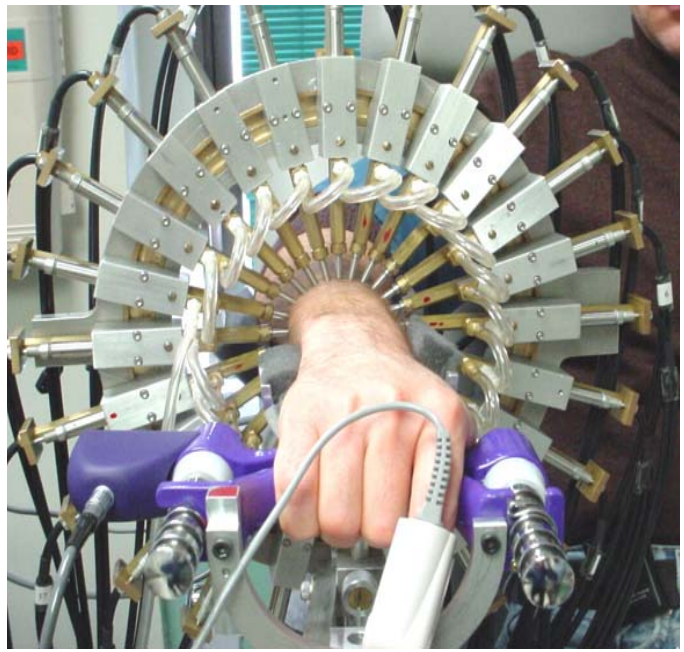

Figure 1. Photograph of dynamic optical imaging system's limb measurement head, with forearm of study subject in place. Each of the 24 optical fibers is both a source (S) and a detector (D); all fiber tips are equidistant from the geometric center (C) of the measurement plane. For any measurement channel, the angle S-C-D is a convenient measure of the distance between source and detector.

Among the operations that currently are routinely performed in the setup stage of a measurment[1]—to assure proper optode-tissue contact for all fibers, or to identify other instrumentational problems—and in the data pre-processing stage of our data analysis package[3]—as a post-measurement data integrity check—are computation of the coefficient of variation (CV) during the baseline period (first 400 seconds of data, in the example shown in Fig. 2) for each channel, application of a low-pass frequency filter to reduce noise levels, and computation of the correlation coefficient (CC) and a normalized root mean squared difference[1] (nRMSD) between all data time series for all pairs of conjugate channels. Examples of the output of these computations, for the experiment that supplied the data shown in Fig. 2, are shown in Figure 3 for the 760 nm illumination wavelength that was used. (Qualitatively similar results were obtained for the second illumination wavelength, 830 nm.) It is seen that, as expected, low-pass filtering significantly impacts the CC and CV surfaces, while having a much smaller effect on the nRMSD results. The filtering operation allows us to conclude, for example, that the apparently poor reciprocity between conjugate pairs with large S-C-D angles is principally a result of the low SNR of those time series, while the low reciprocity seen between the S_{21}-D_{22},S_{22}-D_{21} conjugate pair is an indication of a more serious problem.

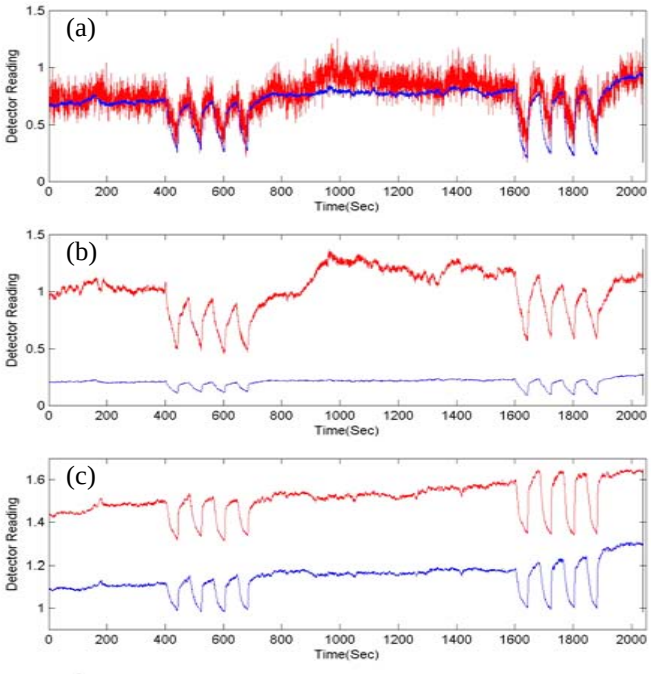

Figure 2. Selected optical tomographic raw-data time series, for 760 nm illumination, obtained using the measurement geometry shown in Fig. 1. Experimental protocol included two sets of four episodes of venous occlusion induced by inflating a blood-pressure cuff placed on the subject's arm, with heating of the arm after the first set. The tracings in 2(a) are time-series recorded by channels with S-C-D angles of 105° (blue) and 135° (red). The pairs of tracings shown in 2(b) and 2(c) are time series recorded by two different sets of conjugate channels, both with 90° S-C-D angles.

The image reconstruction step of the analysis package incorporates two other essential features that are intimately bound up, in practice, with issues of data integrity. First, the systems of equations that are solved to reconstruct the images are formulated by using the Normalized Difference Method[4], which is robust to errors in the "initial guess." However, it is expected that its performance will be degraded by differences between conjugate channels of the type seen in Fig. 2(b), if these are too large. Second, truncated singular value decomposition (tSVD) is used as the solver/optimizer, in large part because it allows the user to fine-tune the degree of regularization by specifying the truncation point. Clearly needed, then, is a method for selecting the optimal truncation point for a specified value of data SNR (or, conversely, for specifying the SNR required in order to allow one to retain the number of singular vectors necessary to successfully reconstruct images with the desired spatial resolution.) Similarly, the question of rigorous methods for choosing a threshold value for the low-pass filter, and CC, CV, and nRMSD computations (above or below what level is a channel or conjugate pair of channels rejected?), all of which have an impact on image quality, must be addressed.

Going beyond these practical considerations, it is known that there are, at least in principle, deficiencies associated with the particular data integrity indices we have employed. For example, a computed CC can be dramatically altered by the presence of even a small number of outliers in the data time series being compared[5]. An important limitation for all three indices is that they combine information from all frequencies into a single number. However, the number of data points in the time series we collect are too small to permit computation of useful frequency-dependent indices such as coherence, but significantly extending the data collection period is not a viable option because (in addition of the practical issue of subject compliance) the requirement that the data be essentially stationary[6] would almost certainly be violated. A worthwhile goal is to seek additional measures of data integrity that, when used in conjunction with those already established, can be more informative and lead to more accurate decisions regarding which data to retain.

Various strategies we are in the process of pursuing to accomplish the goals laid out above are described next.

STRATEGY 1: CHARACTERIZE SENSITIVITY of CC and nRMSD to KNOWN ERRORS

If, for example, the blue curves in Fig. 2 are discarded and replaced by identical copies of the corresponding red ones, then the CC and nRMSD are exactly 1.0 and 0.0, respectively. Then models for different types of measurement error can be introduced in any degree and combination, and their

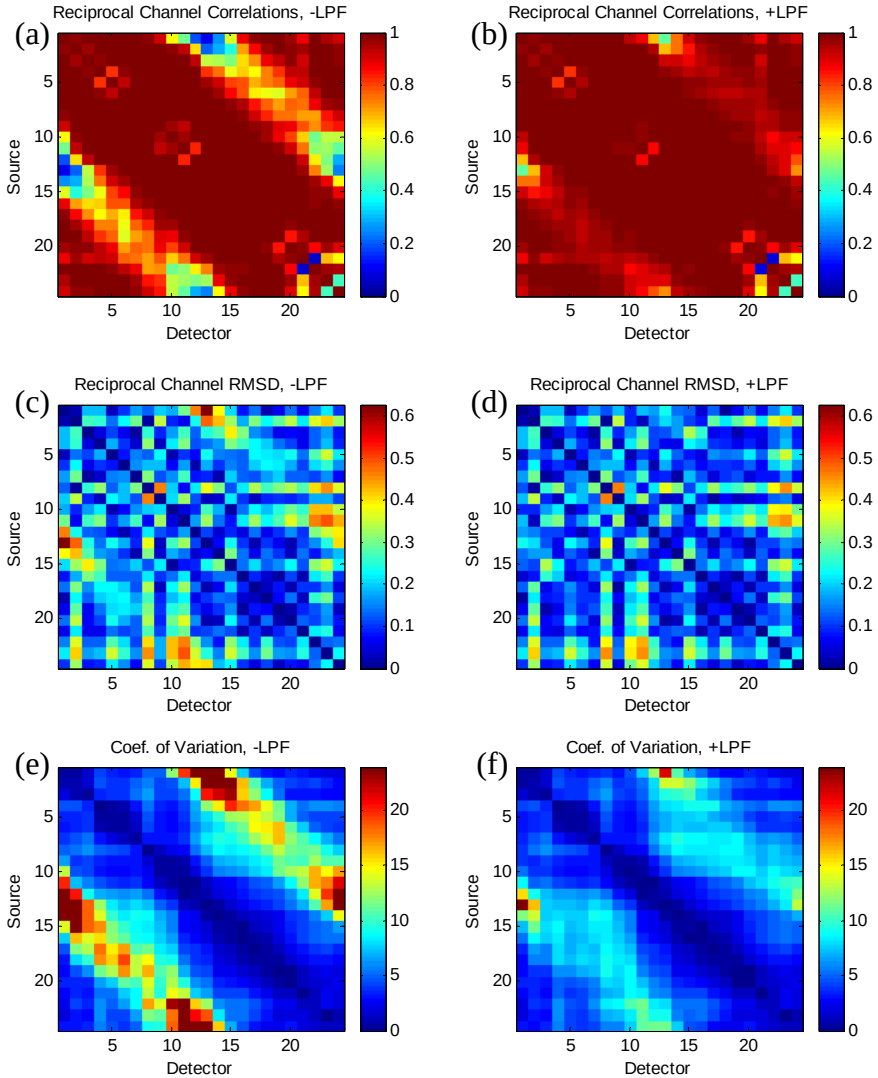

Figure 3. Example of the three data integrity indices routinely computed for dynamic optical tomographic data sets. In this case data were obtained from a forearm measurement. 3(a)-(d): correlation coefficients (3(a),(b)) and normalized root mean squared differences (3(c),(d)) between time series measured in conjugate S-D channels. 3(e),(f): coefficients of variation for the baseline portion of the time series recorded in each channel. Surfaces in 3(a),(c),(e) are results prior to low-pass filtering; 3(b),(d),(f) show results after low-pass filtering with a threshold of 0.15 Hz.

effect on these measures of reciprocity precisely quantified. As a demonstration, this type of analysis was carried out using the data plotted as the red curve in Fig. 2(b) as the starting point, and incorporating four types of commonly encountered measurement error: a constant difference (DC offset error), for which one unit was defined as the mean value of the unperturbed time series; a constant ratio (Scale Factor); Additive Noise (Gaussian), for which one unit was defined as the standard deviation of the unperturbed time series; and Multiplicative Noise (Gaussian). Plotted in Figure 4 are surfaces illustrating the dependence of CC on the magnitudes of both types of noise, and the dependence of nRMSD on the offset and scale errors. In each of these cases the two control parameters included in the plot are the ones to which the respective response variable is most sensitive, while the remaining two are set to zero. Inspection of surfaces of these types allow us to determine what ranges of all modeled error types are consistent with a CC value of at least, say, 0.8, or a nRMSD of at most, say, 0.3. (These specific values, which have tentatively been chosen as the acceptability thresholds for forearm measurement data, correspond to the red contours on the baseplanes of Fig. 4.) The range of variability of the CC and nRMSD with all four modeled error types is indicated in Figure 5, where the indices are plotted against only one of the four control parameters, and each of the 125 data points (open diamond symbols) at each position along the abscissa is a CC (Fig. 5(a)) or a nRMSD (Fig. 5(b)) computed for one of the possible permutations of the other three error types.

STRATEGY 2: SYNCHRONY INDEX COMPUTATION; DECISION TREE

The principal novelty here is that the set of data integrity indices already considered is augmented by the computation of an additional one, i.e., the phase synchrony index[7] (SI), a wavelet-based technique applicable to non-stationary time series. By convolving the measurement time series for a conjugate pair of S-D channels with a scaled wavelet (the order-2 Coifman wavelet, sketched in Figure 6, was used here), only variations occurring on a time scale comparable to a frequency of interest are selected. The pair of time series obtained at each frequency are demodulated (i.e., their Hilbert

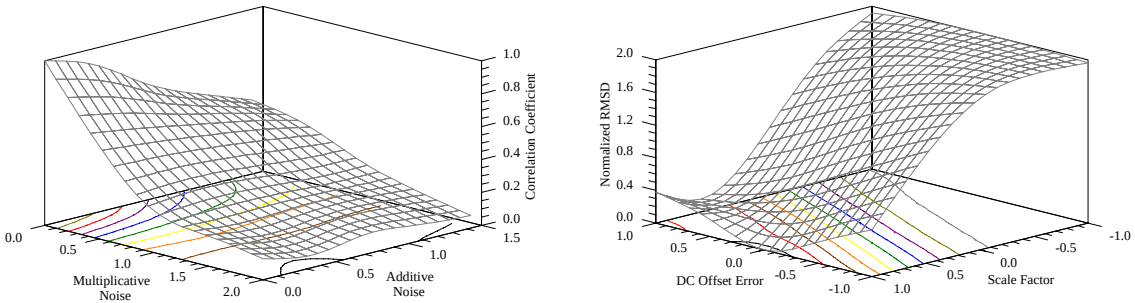

Figure 4. 4(a): response surface for the dependence of CC on the magnitudes of additive and multiplicative noise in one member of a pair of conjugate-channel time series, with zero DC offset error and zero scale error. 4(b): response surface for the dependence of nRMSD on the magnitudes of DC offset error and scale error in one member of a pair of conjugate-channel time series, with zero additive noise and zero multiplicative noise.

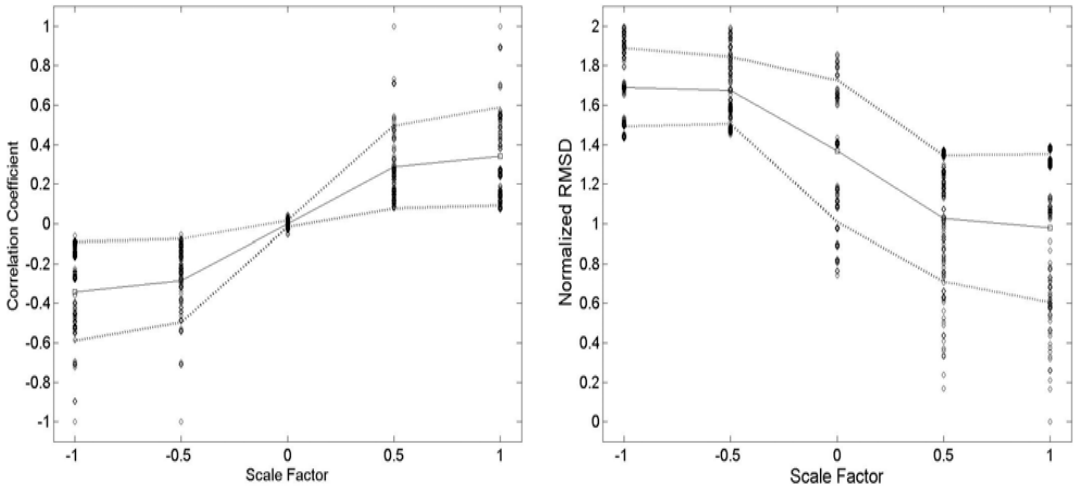

Figure 5. 5(a): scatter plot of all CC values computed, at each Scale Factor value, for all combinations of the remaining three model error types. 5(b): scatter plot of all nRMSD values computed, at each Scale Factor value, for all combinations of the remaining three model error types. Solid lines, open square symbols, indicate the mean value of CC or of nRMSD at each Scale Factor value, while the dotted lines pass one standard deviation above and below the mean.

transforms are computed, the transforms are multiplied with a complex exponential having the frequency of interest, and the phase of the product is extracted), and the difference between the phases of the two series is taken at all time points. The SI is a measure of the degree to which the phase difference varies over time. An illustration of the utility of this index is shown in Figure 7, where the red and blue curves in the top panel are noisy phase-modulated sine waves with a common carrier frequency and common initial phase, and, starting at the 250-second mark, a 500-point segment of one was substituted with a 90° phase-shifted copy of the other. It was predicted analytically that the SI should be 0.6 for this situation, and the numerically computed SI plotted in the lower panel of Fig. 7 shows a rapid drop to near the predicted value after 250 seconds.

Comparison of a large set of SI values with the experimental time series from which they were derived has led to a tentative acceptance of 0.9 as a threshold value, below which data from conjugate S-D channels should be judged unequal, at the time scale(s) used in the SI computations. Illustrative examples drawn from experimental data are shown in Figure 8. In one case the SI is slightly greater than 0.9, and the difference between the phases of the two signals being compared is smaller than either of them, in terms of both magnitude and duration of the “blips” in Fig. 8(b). In the other case, $0.8 < SI < 0.9$, and the difference between the phases is comparable in magnitude to those of the signals being compared.

The addition of SI to the CC and nRMSD computations already performed allowed us to empirically derive the decision tree, shown in Figure 9,

for the case of forearm measurements, that has two important uses. First (portions of Fig. 9 boxed in red), it can be incorporated into the software that controls the data acquisition process, for automatic flagging of S-D channels where poor fiber-skin contact is probable. Second, it can be incorporated into the data processing software package, to identify channels that should be excluded from image reconstruction operations on the grounds of failing to exhibit the expected degree of reciprocity.

An additional potential benefit of the SI is that it should allow us to derive a rigorous answer to one of the remaining problems from the list set out above: determination of an optimal value for low-pass filter thresholds. The idea is to conduct rapid (i.e., single-source) data collection, which will permit computation of SI values on much shorter time scales (i.e., out to higher frequencies) than is possible using full-tomographic measurement data. It is expected that, as shown as a sketch in Figure 10, the SI will decrease with increasing frequency, and that the frequency at which it begins to drop off rapidly will decrease with increasing S-C-D angle. The frequency at which the SI falls below 0.9 will be taken as an upper limit for the low-pass filter threshold for S-D channels having the corresponding angle.

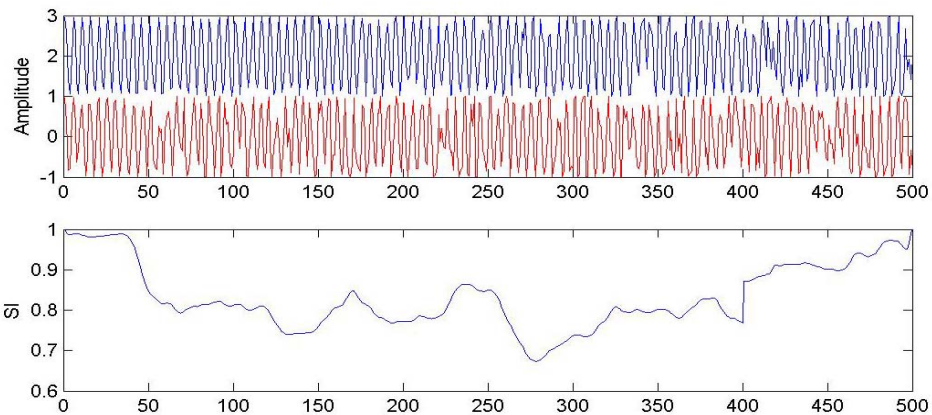

Figure 7. Numerical demonstration of utility of SI for gauging similarity between time series. Top: noisy phase-modulated sine waves with a common carrier frequency and common initial phase. Starting at the 250-second mark, a 500-point segment of one was substituted with a 90° phase-shifted copy of the other. Bottom: numerically computed SI at the carrier frequency.

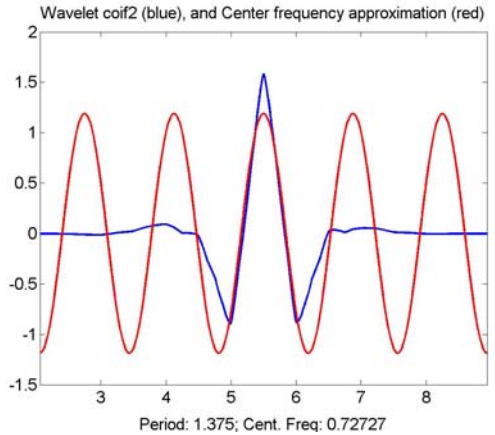

Figure 6. "Mother wavelet" of the order-2 Coifman family (blue), and a sine wave at its central frequency (red).

STRATEGY 3: FINDING OPTIMAL TRUNCATION POINT for tSVD

For a dynamic optical tomographic data set, it is useful to compare the temporal trend of the spatially averaged optical coefficients according to the reconstructed images to that obtained directly from the S-D channel data. An example of such a comparison, in this case carried out for a portion of a time series of data collected in a 3D optical mammography experiment, is shown in Figure 11. Here the temporal response at the 760 nm measurement wavelength, averaged over all S-D channels, is plotted as a green curve, and the temporal response in the reconstructed images, for the indicated numbers of singular vectors (SVs) included and averaged over all image pixels, are plotted as blue curves. It is clear from these results that retention of more than 100 SVs in the tSVD computation results in image quality degradation. The degree of similarity between the shapes of the blue and green curves in Fig. 11 was quantified by computing the RMSD between them; this difference is plotted vs. the number of SVs retained by the reconstruction algorithm, for both measurement wavelengths, in Figure 12. One possibly significant observation is that the truncation point at which the RMSD has its absolute minimum is different for the two wavelengths. In addition, these results have led us to expect that a generally useful (i.e., also applicable to cases where no provocation is employed)

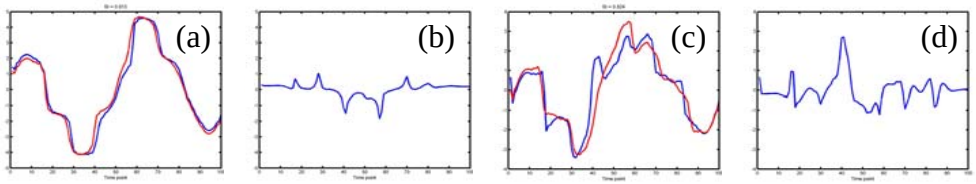

Figure 8. Examples of phase modulations (8(a),(c)) and phase modulation differences (8(b),(d)) obtained from experimental data time series recorded in particular conjugate pairs of S-D channels. For the example shown in 8(a),(b), the computed SI is 0.913; for the example shown in 8(c),(d), SI = 0.824.

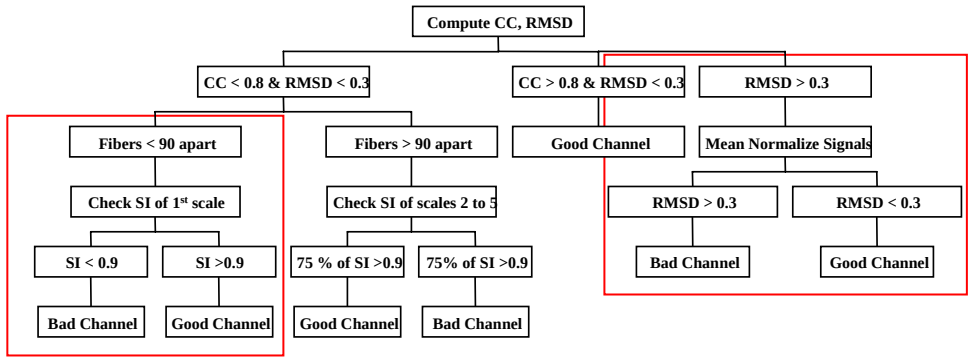

Figure 9. Empirically derived decision tree for determining which fibers have probable poor contact with skin during experimental setup stage (red boxed regions) and which pairs of channels should be excluded from image reconstruction stage of data processing (entire chart).

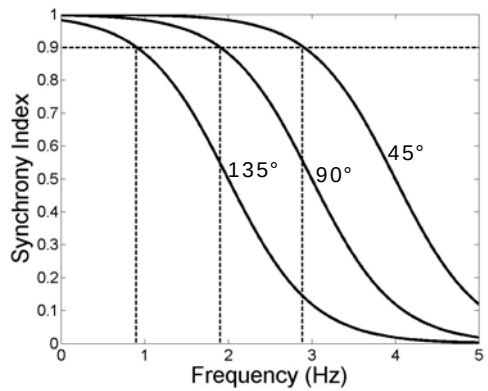

Figure 10. Sketch illustrating proposed application of SI computation to the problem of determining optimal low-pass filter thresholds.

strategy for finding the optimal truncation point is to seek equal spatiotemporal variance between the detector and image data, as indicated by the conjectural sketch in Figure 13.

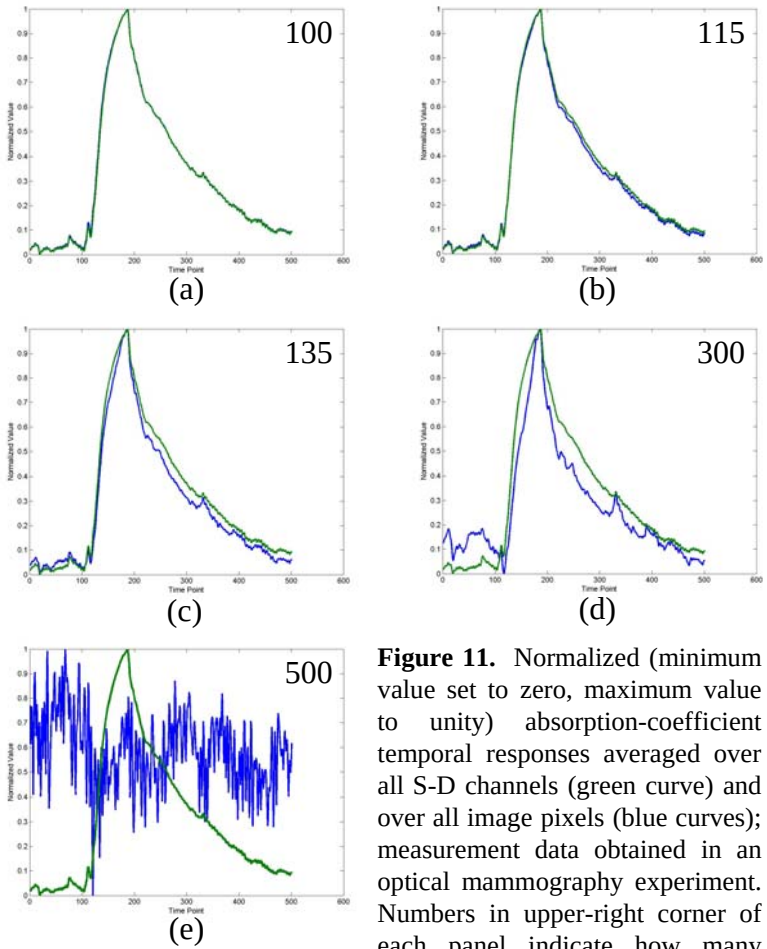

Figure 11. Normalized (minimum value set to zero, maximum value to unity) absorption-coefficient temporal responses averaged over all S-D channels (green curve) and over all image pixels (blue curves); measurement data obtained in an optical mammography experiment. Numbers in upper-right corner of each panel indicate how many singular vectors were included in the image reconstruction computations.

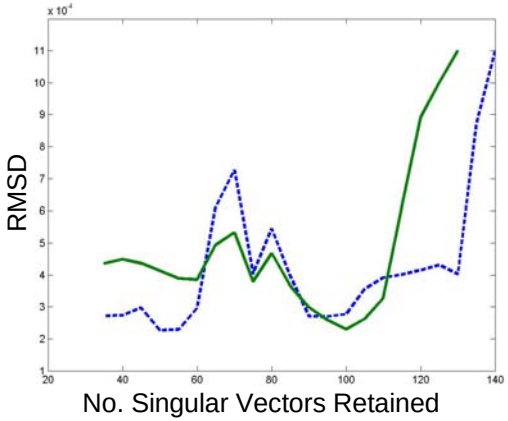

Figure 12. Root mean squared differences between time-varying (see Fig. 11) spatially averaged absorption coefficients in images and in detector data, vs. number of singular vectors included in image reconstructions, for 760 nm (green) 830 nm (blue) illumination wavelengths.

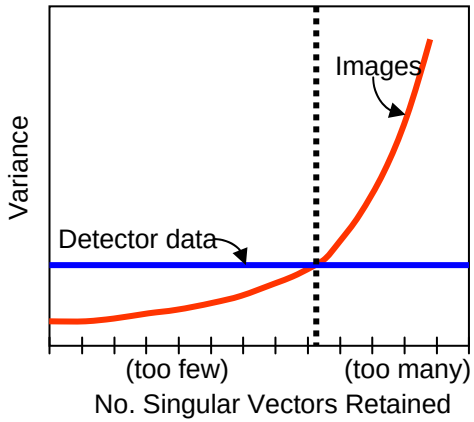

Figure 13. Suggestion for generally applicable method for determining optimal tSVD truncation point. Images will have lower spatiotemporal variance than detector data if too few singular vectors are retained, and higher variance if too few are discarded.

CONCLUSION

The availability of robust data integrity checking procedures is an essential part of any practical diffuse optical tomography (DOT) system, and one that may not have not received sufficient attention in the past. The use of co-located sources and detectors and collection of time-series data are features of our imaging system that permit the use of the particular data integrity testing methods we have employed. The data integrity indices used by our software for processing dynamic DOT time series will, when their performance is thoroughly characterized through the sorts of analysis described here, allow us to quantitatively assess the reliability of experimental or clinical measurement data. Thus the reliability of images and dynamic feature maps also will become quantifiable.

REFERENCES

1. C. H. Schmitz, H. L. Graber, R. D. Levina, M. B. Levin, R. L. Barbour, "Data integrity assessment and instrument calibration for the DYNOT imaging system," *OSA Biomedical Optics Topical Meetings, Advances in Optical Imaging and Photon Migration* (Miami Beach, FL, April 14-17, 2004).

2. J. R. Lamarsh, *Nuclear Reactor Theory* (Addison-Wesley, Reading, MA, 1966).

3. Y. Pei, H. L. Graber, Y. Xu, R. L. Barbour, "dynaLYZE—an analysis package for time–series NIRS imaging data," *OSA Biomedical Optics Topical Meetings, Advances in Optical Imaging and Photon Migration* (Miami Beach, FL, April 14-17, 2004).

4. Y. Pei, H. L. Graber, R. L. Barbour, "Influence of systematic errors in reference states on image quality and on stability of derived information for DC optical imaging," *Applied Optics* **40**, 5755-5769 (2001).

5. H. M. Wadsworth, *Handbook of Statistical Methods for Engineers and Scientists* (McGraw-Hill, New York, 1990).

6. J. S. Bendat, A. G. Piersol, *Engineering Applications of Correlation and Spectral Analysis*, 2nd Ed. (Wiley, New York, 1993).

7. J.-P. Lachaux, E. Rodriguez, J. Martinerie, F. J. Varela, "Measuring phase synchrony in brain signals," *Human Brain Mapping* **8**, 194-208 (1999).

ACKNOWLEDGMENTS

This work was supported by the National Institutes of Health (NIH) under Grants R21-HL67387, R21-DK63692, R41-CA96102 and R43-NS49734, and by the US Army under Grant DAMD017-03-C-0018.